### Title

Neonate and infant brain development from birth to 2 years assessed using MRI-based quantitative susceptibility mapping




### Authors

Zhang, Yuyao
Shi, Jingjing
Wei, Hongjiang
et al.



### Publication Date

2019

### DOI

10.1016/j.neuroimage.2018.10.031

Peer reviewed

HHS Public Access

Author manuscript

*Neuroimage*. Author manuscript; available in PMC 2020 January 15.

Published in final edited form as:

*Neuroimage*. 2019 January 15; 185: 349–360. doi:10.1016/j.neuroimage.2018.10.031.

# Neonate and Infant brain development from birth to 2 years assessed using MRI-based quantitative susceptibility mapping

**Yuyao Zhang**[#1], **Jingjing Shi**[#2], **Hongjiang Wei**[3], **Victor Han**[3], **Wen-Zhen Zhu**[2,*], and **Chunlei Liu**[3,4,*]

[1]School of Information and Science and Technology, ShanghaiTech University, Shanghai, China

[2]Department of Radiology, Tongji Hospital, Tongji Medical College, Huazhong University of Science and Technology, Wuhan, China

[3]Electrical Engineering and Computer Science, University of California at Berkeley, CA, USA

[4]Helen Wills Neuroscience Institute, University of California at Berkeley, CA, USA

[#] These authors contributed equally to this work.

## Abstract

The human brain rapidly develops during the first two years following birth. Quantitative susceptibility mapping (QSM) provides information of iron and myelin variations. It is considered to be a valuable tool for studying brain development in early life. In the present work, QSM is performed on neonates, 1-year and 2-year old infants, as well as a group of adults for the purpose of reference. Age-specific templates representing common brain structures are built for each age group. The neonate and infant QSM templates have shown some unique findings compared to conventional T1w and T2w imaging techniques. The contrast between the gray and white matters on the QSM images did not change through brain development from neonate to adult. A linear correlation was found between brain myelination determined in this study and the microscopic myelin degree determined by a previous autopsy study. Also, the magnetic susceptibility values of the cerebral spinal fluid (CSF) exhibit a gradually decreasing trend from birth to 2 years old and to adulthood. The findings suggest that the macromolecular content, myelin, and iron may play the most important contributing factors for the magnetic susceptibility of neonate and infant brain. QSM can be a powerful means to study early brain development and related pathologies that involve alterations in macromolecular content, iron, or brain myelination.

## 1. Introduction

The first 2 years of life are the most dynamic and critical phase of postnatal brain development. The study of healthy neonate and infant brain development is essential to

[*]Corresponding author: Chunlei Liu, PhD, Wen-Zhen Zhu, PhD MD, Electrical Engineering and Computer Science, University of California at Berkeley, 505 Cory Hall, MC #1770, Berkeley, CA 94720, chunlei.liu@berkeley.edu, Phone: 510-664-7596.

understand early cognitive and motor development, as well as potential pathogenesis of neurodevelopmental disorders. The anatomical characteristics of gray matter (GM) and white matter (WM) developmental processes have been documented in studies of postmortem fetus, neonate and infant brains (Brody, Kinney et al. 1987, Kinney, Brody et al. 1988, Huang, Zhang et al. 2006, Kolasinski, Takahashi et al. 2013). Previous studies have suggested that by full-term birth, all major fiber systems are in place (Huang, Zhang et al. 2006, Kolasinski, Takahashi et al. 2013), but the central nervous system (CNS) myelination occurs only in a few sites, mostly distributed in the cerebellum, midbrain, pons, medulla and spinal cord (Brody, Kinney et al. 1987, Kinney, Brody et al. 1988). Brody et al. established the sequence of myelination in a population of autopsied infants from birth through the second postnatal year. The authors assessed myelination in sixty-two anatomic sites from the brain and spinal cord using an ordinal scale of degrees 0–4 (Brody, Kinney et al. 1987, Kinney, Brody et al. 1988). In neonate brains, only 0.5–1 degrees of myelin were observed in the sampled sites and only a few sites achieved the degree of 4, and most of the WM myelination is still incomplete by the second postnatal year. The myelination progression is asynchronous, it follows a caudo-rostral gradient and progresses from the center to periphery.

Magnetic resonance (MR) imaging has significantly advanced the interpretation of brain development and maturational processes that take place after birth. Using structural T1-weighted (T1w) and T2-weighted (T2w) MRI techniques, Knickmeyer et al. (Knickmeyer, Gouttard et al. 2008) identified that the total brain volume increases by 101% in the first year and by 15% in the second year. This vigorous growth in the first year of life was mainly driven by the GM growth. While WM grows more slowly than GM in terms of size, as the volume of hemispherical white matter increases by only 11% in the first year and by 19% in the second year (Knickmeyer, Gouttard et al. 2008). The early maturation of white matter, particularly myelination, is a complex and fast-growing process (Knickmeyer, Gouttard et al. 2008). Myelination starts late in embryonic development and continues through postnatal life. The neonatal and infantile pattern (0–6 months) on T1w and T2w show poor contrast between GM and WM, the contrast is actually reversed compared to adults. The changes observed on T1w and T2w contrasts can be used to understand maturation processes, but T1w and T2w signals cannot be directly compared across individuals because of the variability between exams related to technical tunings (Dubois, Dehaene-Lambertz et al. 2014).

Many investigators have used diffusion tensor imaging (DTI) to investigate microstructural changes in white matter at different stages of brain development and their relationship to cognitive ability in early life (Gilmore, Lin et al. 2007, Dubois, Dehaene-Lambertz et al. 2008, Qiu, Mori et al. 2015). DTI studies were conducted to identify multiple neural structures during the fetal period. Researchers have shown that the Sylvia fissure and temporal lobe are visible at 19–20 post conceptual weeks. All major fiber systems are in place by term birth. Although DTI offers insight into structural maturation, it reflects several different facets of development, e.g., changes in axonal size, density, coherence, and membrane structure; lipid, protein, and macromolecule content; and water compartmentalization (K. and Mara 2010, Jones, Knösche et al. 2013). Consequently, observed signal changes are ambiguous, hindering meaningful inferences between imaging

findings and metrics of learning, behavior or cognition (Beaulieu 2002, Qiu, Mori et al. 2015). Using a myelin-specific MRI technique called myelin water fraction (MWF), Deoni et al. proposed a noninvasive quantitative measure of myelin content in the brains of healthy infants between 3 and 11 months of age (Deoni, Mercure et al. 2011, Deoni, Dean et al. 2012). Reconstructing average myelination trajectories across different brain regions, MWF is reported drastically increases during WM maturation. As for approaches based on "multi-component relaxation" (MCR) analyses, different pools of water molecules are modeled in each voxel. Such decomposition is supposed to provide valuable information on the tissue microstructure. Whereas the exact number of pools to be modeled is debated (Deoni, Matthews et al. 2013), making direct comparisons across studies challenging.

Quantitative susceptibility mapping (QSM) is a relatively new MRI technique that measures the spatial distribution of magnetic susceptibility within biological tissues (Deistung, Rauscher et al. 2008, de Rochefort, Liu et al. 2010, Liu 2010, Wharton, Schäfer et al. 2010, Liu, Li et al. 2012, Dibb, Xie et al. 2017, Wei, Dibb et al. 2017, Wei, Gibbs et al. 2017). The previous works have proposed models to evaluate the QSM sensitivity to encapsulate the full repertoire of signal behavior (Chen, Foxley et al. 2013). Since magnetic susceptibility is sensitive to iron and myelin in the brain, QSM can be another imaging technique used as a marker of iron deposition in the deep gray matter (DGM) and myelination in the WM (Shmueli, de Zwart et al. 2009, Haacke, Miao et al. 2010, Carpenter, Li et al. 2016, Wei, Xie et al. 2016, Cronin, Wang et al. 2017). In the early developmental neural system, iron is an essential trophic factor required for myelination (Connor and Menzies 1996). Iron-containing oligodendrocytes are found near neuronal cell bodies and are particularly abundant within WM tracks in the neonatal rat brain (Connor, Pavlick et al. 1995, Cheepsunthorn, Palmer et al. 1998). The sensitivity of QSM to myelin and iron provides an exclusive way to investigate the WM maturation in the neonate and infant brain. In this study, QSM is performed on normal full-term neonates and infants (birth to 2 years of postnatal age), as well as a group of adults for the purpose of reference. Age-specific templates are built for each age group using a group-Myelin and iron concentration in the human brain: A quantitative study of MRI contrast.wise registration process. The average templates, which emphasize the common structures and smooth out individual characteristics, represent global development for the population. Combined with T1w and R2* image templates, we quantify the structural development during the neonatal and infantile brain maturation process and discuss the unique findings in WM, DGM and cerebral spinal fluid (CSF).

## 2. Method

### 2.1. Data Acquisition

Twelve neonate subjects (5M/7F), ten 1-year-old infant subjects (4M/6F) and eleven 2-year-old infant subjects (6M/5F) were scanned using a 3T GE MR750 scanner (GE Healthcare, Waukesha, WI) with following parameters: repetition time (TR) = 50 ms, echo time $(TE)_1$/spacing/$TE_{16}$ = 2.9/2.9/46.4 ms, field of view (FOV) = 220×220 $mm^2$, number of slices = 136, and spatial resolution = 1×1×1 $mm^3$, matrix size = 220 × 220, SENSE factor of 2, scan time =12 mins. The neonate subjects included both early-term (delivered between 37 weeks

0 day through 38 weeks 6 days) and full-term (delivered between 39 weeks 0 days through 40 weeks 6 days) babies (Spong 2013) and were scanned 1–7 days after birth. The 1-year-old subjects were full-term infants who were scanned between 20–24 gestation months. The 2-year-old subjects were full-term infants who were scanned between 32–35 gestation months. The neonates and infants were scanned without being sedated and were fed before scanning. Infant earmuffs were used for hearing protection, and possible motion artifacts were mitigated by immobilization with a cotton pillow. An experienced neonatologist and a neuroradiologist were in attendance throughout the imaging process. A pulse oximeter was used to monitor heart rate and oxygen saturation. The 12 adult subjects (age 33–40 years, 8M/4F) were scanned at the Brain Imaging and Analysis Center (BIAC) at Duke University, using a GE MR750 3T with the following scan parameters: $TE_1$/spacing/$TE_8$ = 5/2.94/25.6 ms, TR = 55 ms, and spatial resolution = 1×1×1 $mm^3$. Imaging was carried out with the approval of the institutional review board and informed consent from the adult subjects and parental consent for babies. All included subjects met the following radiological imaging criteria: (1) normal appearance on conventional MRI and (2) no obvious motion artifacts or an incomplete imaging process.

T1 weighted data were acquired using IR-prepared fast Spoiled gradient echo (FSPGR) sequence with the following parameters: inversion time = 900ms, TI/TR/TE=950/3000/23 ms, FOV = 220×220 mm, matrix size = 220×220, slice thickness = 1mm, slice number = 132, flip angle 8, voxel size: 1×1×1 $mm^3$

## 2.2. Data processing

### 2.2.1 Image Reconstruction

**QSM reconstruction.:** QSM reconstruction was performed in STI Suite V3.0 (https://people.eecs.berkeley.edu/~chunlei.liu/software.html). The sum of squares of gradient echo (GRE) magnitude images across echo times $\left(\sum_{i=1}^{n} mag_i^2, i = 1, 2, \ldots, n\right)$, where n is the number of echoes, was used to mask and extract the brain tissue using the brain extraction tool (BET) in FSL (Smith, Jenkinson et al. 2004). The raw phase was unwrapped using a Laplacian-based phase unwrapping (Schofield and Zhu 2003). The normalized phase $\psi$ was calculated as $\psi = \frac{\sum_{i=1}^{n} \omega_i}{\gamma \mu_0 H_0 \sum_{i=1}^{n} TE_i}$, where ω is unwrapped the phase. The normalized background phase was removed with the spherical mean value (SMV) method (Schweser, Deistung et al. 2011, Wu, Li et al. 2012). The variable radius of the SMV filter increased from 1 pixel at the brain boundary to 25 towards the center of the brain with a truncated singular value decomposition of 0.05 for the SMV filter during the deconvolution process (Wu, Li et al. 2012). Lastly, susceptibility maps were computed by inversing the filtered phase using the STAR-QSM algorithm (Wei, Dibb et al. 2015, Wei, Zhang et al. 2016). Susceptibility values were not explicitly referenced to any region of interest since previous studies on brain aging by QSM have shown that no obvious systematic bias is observed between analysis with and without referencing to CSF (Li, Wu et al. 2014, Zhang, Wei et al. 2018).

**R2* map calculation.:** R2* maps were calculated by fitting the signal intensity decay with a mono-exponential model using the following expression: $S(t) \cong S(0) \cdot \exp(-\frac{TE}{T2^*}) + C$, where S(t) is signal intensity at time t, S (0) is the initial signal intensity, TE is echo time, and C is the offset.

**2.2.2 Average age-specific template computation—**For each age group, a group-wise registration strategy (Wu, Jia et al. 2010, Wu, Jia et al. 2011, Zhang, Shi et al. 2016, Zhang, Shi et al. 2016) was implemented as shown in Fig. 1. Specifically, the QSM images with the same age were aligned to form an *age-specific template image*. All the individual QSM are firstly linear aligned to a chosen subject, using FSL affine registration (FLIRT) (Smith, Jenkinson et al. 2004), with DOF 12, cost function "Correlation Ratio", to form the initial average template space. Due to the variations among subjects, the initialization is a blurry average image. And later all the individual images are non-linearly aligned to the average template built in the previous iteration, using diffeomorphic registration (DEMONS) (Vercauteren, Pennec et al. 2009), with cost function "Correlation Ratio". The average anatomy $\bar{I}_{QSM}(i)$ of a certain age group was then calculated iteratively by:

$$\bar{I}_{QSM}(i+1) = \frac{1}{N}\sum_{n=1}^{N} I_{QSMn} \circ \varphi_n(i) \quad (1)$$

where $\circ$ represents the operation of performing the deformation field $\psi_n(i)$ on the individual QSM image $I_{QSMn}$ for the *(i+1)-th* iteration. The deformation fields $\psi_n(i)$ are produced by the pair-wise registration procedure, which aligns the individual image $I_{QSMn}$ towards the average anatomy $\bar{I}_{QSM}(i)$ generated in the *i-th* iteration (Wu, Jia et al. 2010, Wu, Jia et al. 2011). For generating the R2* template $\bar{I}_{R2*}$ the deformation fields $\psi_n$ are performed on each individual R2* image, respectively.

Furthermore, the T1w images were then co-registered to the corresponding magnitude images using FSL FLIRT (Smith, Jenkinson et al. 2004), with DOF 12, cost function "mutual information". Thus, the individual QSM images and T1w images were placed in the same space. Then we propagated deformation fields $\varphi_n$ on the individual T1w images to generate the related average T1w age-specific template $\bar{I}_{T1-W}$.

**2.2.3 Neonate and infant brain segmentation based on template—**Using the T1w templates at each specific age, we registered the JHU T1w infant atlas (Oishi, Mori et al. 2011) to each neonate and infant QSM template space to generate brain parcellation.

Firstly, the JHU T1w infant atlas was registered towards the proposed T1w infant template via FSL affine registration (FLIRT) (Smith, Jenkinson et al. 2004) followed by diffeomorphic registration (DEMONS) (Vercauteren, Pennec et al. 2009). The deformation fields were then applied to the 122 regions of interests (ROIs) infant brain parcellation (Oishi, Mori et al. 2011) to warp the cortical and WM fiber bundle ROIs onto the infant QSM template.

## 2.3. Data analysis

### 2.3.1 Neonate and infant brain susceptibility evolution in the white matter fiber bundles

**Volume-of-interested identification:** Previous studies have demonstrated that magnetic susceptibility is substantially affected by variations in myelin density in the brain tissue (Liu, Li et al. 2011, Lee, Shmueli et al. 2012), as the proteins and lipids associated with myelin render its susceptibility diamagnetic. In the myelination sequence study (Brody, Kinney et al. 1987, Kinney, Brody et al. 1988), Brody *et al.* assessed myelination in 62 precisely defined CNS sites of 162 neonates and infants. The study pool included full-term newborn (>37 weeks gestation) to 33 months post-conceptional age (gestational age plus postnatal age, equivalent to 2-year postnatal age). Using a visual ordering from stages 0 to 4 according to staining, researchers established that the sequence of myelination followed a caudorostral gradient and progresses from the center to the periphery (Kinney, Brody et al. 1988).

In our work, we take the myelination sequence work as a guideline to evaluate the effect of myelination on the susceptibility in neonate and infant brain WM fibers. WM fibers are annotated using the whole brain parcellation map generated in Sec. 2.4. The susceptibility values in the following WM fiber bundles are extracted and correlated with the microscopic myelination degrees (Brody, Kinney et al. 1987) accordingly: body corpus callosum (BCC); splenium corpus callosum (SCC); external capsule (EC); middle cerebellar peduncle (MCP); cerebral peduncle (CP); posterior thalamic radiation (PTR); corona radiate (CR); pontine crossing tract (PCT); medial lemniscus (ML); corticospinal tract (CST); posterior limb of internal capsule (PLIC).

**Statistical analysis:** Linear regression of the mean susceptibility as a function of the microscopic myelination degrees was generated as the following using MATLAB (The Mathworks, Inc., Natick, MA, USA):

$$\chi[ppm] = Slope \cdot myelin[degree] + offset[ppm] \quad (2)$$

where $myelin\,[degree]$ is the microscopic myelination degree defined in (Brody, Kinney et al. 1987) and the susceptibility value $\chi$ [ppm] is referenced to the mean susceptibility of selected white matter fibers.

### 2.3.2 Development of R2* and magnetic susceptibility with age in deep brain nuclei and white matter fiber bundles

**Volume-of-interested identification:** To investigate the development trajectory of R2* and susceptibility, volumes-of-interest (VOIs) were defined in both hemispheres. Based on the atlas segmentation, VOIs of the DGM nuclei, i.e. putamen (PT), globus pallidus (GP) and caudate nucleus (CN), and WM fiber bundles, i.e. Corticospinal tract (CST), posterior limb of internal capsule (PLIC) and posterior thalamic radiation (PTR) for each individual neonate, infant and adult brain were extracted, respectively.

**Fitting susceptibility and R2* development in the deep gray matter nuclei.:** Progressive accumulation of iron with aging has been well reported in brain tissues (Hallgren and Sourander 1958). Since iron is the main contributors of both R2* and magnetic susceptibility contrast in deep gray nuclei (Schweser, Deistung et al. 2011), the susceptibility and R2* development in DGM regions can be modeled using the exponential growth model (Li, Wu et al. 2014), which was originally proposed by Hallgren et al. (Hallgren and Sourander 1958):

$$observation = \alpha(1 - exp(-\beta * age[year])) + \gamma \quad (3)$$

where *observation* represents either the magnetic susceptibility or the R2* relaxation rate, the scalar variables $\alpha$, $\beta$ and $\gamma$ are tissue specific parameters, with $\beta$ defining the rate of the exponential growth.

**Fitting susceptibility and R2* development in the white matter fiber bundles.:** Previously, Lebel et al. (Lebel, Gee et al. 2012) investigated the changes in DTI fractional anisotropy (FA) and mean diffusivity (MD) of 12 major white-matter connections aged 5–83 years, and modeled the trajectories of FA and MD using Poisson curves (Lebel, Gee et al. 2012). In the WM fiber bundle VOIs, we tested similar behavior of magnetic susceptibility and R2* measurements following:

$$observation = M \times age \times \exp(-age * N) + K \quad (4)$$

where *observation* represents either the magnetic susceptibility or the R2* relaxation rate, the scalar variables $M$, $N$ and $K$ are tissue specific-parameters.

**Correlation of R2* and magnetic susceptibility in deep brain nuclei and white matter fiber bundles:** Finally, the mean R2* and susceptibility of the VOIs were correlated and investigated statistically using MATLAB (The Mathworks, Inc., Natick, MA, USA) following equation:

$$\mathrm{R2}^*\left[\mathrm{s}^{-1}\right] = \mathrm{Slope}\left[\mathrm{ppb}^{-1}\mathrm{s}^{-1}\right] \cdot \chi[\mathrm{ppb}] + \mathrm{offset}\left[\mathrm{s}^{-1}\right]. \quad (5)$$

Pearson's correlation coefficients were computed. If the magnitude of Pearson's correlation coefficient exceeded 0.5, a linear weighted total least-square regression was performed with the means of the respective VOIs (Krystek and Anton 2008). One-way analysis of covariances (ANCOVA) (Bingham and Fry 2010) was performed to assess the significance of the regression coefficients. A p-value below 0.001 was considered statistically significant.

# 3. Results

## 3.1. Age-specific templates for neonate and infant brain

**3.1.1 Qualitative analyses—**Fig. 2 shows the age-specific T1w, R2* and QSM templates for different groups. In the T1w and R2* (Fig.2 (a) & (b)) neonate templates, the contrast between GM and WM is inverted compared to later ages. After 1-year-old, the basic contrast characteristics on the T1w and R2* maps do not change and the R2* values in both WM and GM increase as age increases. The rate of increase of R2* for GM is slower than that for WM, thus leading to reduced contrast between GM and WM. Minor variation in deep brain nuclei was observed on R2* images from neonates to 1 and 2-year-old infants. In the adult brain template on the other hand, the R2* values in the deep brain nuclei are much higher than those in baby brains. Interestingly, the susceptibility contrast between gray and white matter is relatively low compared to later ages (Fig.2 (c)). From neonates to 2-year-old, the contrast between GM and WM in QSM templates shows remarked increase; the susceptibility shows substantial increases in globus pallidus (GP), putamen (PT) and caudate nuclei (CN) but are still much lower than that in adult brains.

**3.1.2 Magnetic susceptibility and R2* development with age—**In Fig. 3, the mean susceptibility and R2* values in the selected DGM and WM regions of all individual subjects are scatter plotted as a function of monthly gestation age. The left column indicates the global development trajectory through neonate, infant and adult, while the right column shows the close-view for development trajectory at early age (for neonate and infant). Using the exponential growth model (Eq. 3) to fit the susceptibility and R2* development with age in the DGM, the fitted curves are given by: $\chi = 78.05 * (1 - e^{-0.012*Age}) - 9.56$ and $R2^*(\chi) = 59.78 * (1 - e^{-0.0056*Age}) + 5.07$, denoted via red fitted curve in the top and bottom rows, respectively. For investigating variations related to WM development, susceptibility and R2* estimates are modeled using Poisson curve (Eq. 4). The fitted lines are given by: $\chi = -0.45 * Age * e^{-0.0027*Age} + 0.73$ and $R2^*(\chi) = 0.25 * Age * e^{-0.0031*Age} + 8.12$, indicated in purple dotted lines in top and bottom rows respectively.

**Correlation between bulk susceptibility and R2*:** The results of the linear regression analysis of R2* and susceptibility are summarized in Table S1. Considering the selected DGM and WM regions of all subject samples (neonate, infant and adult), R2* showed a positive linear correlation with the magnetic susceptibility, but not well fitted model (Table S1 row 1; r=0.539, p<0.001, $R^2$=0.191). The linear correlation increased substantially when white matter regions were excluded from the analysis. The strongest linear correlation was obtained for infant & adult DGM regions (Table S1 row 4; r=0.93, p<0.001, $R^2$=0.870). R2* showed significant negative linear correlation with susceptibility in WM regions (Table S1 row 3; r=−0.742, p<0.001, $R^2$=0.551). A stronger linear correlation was observed when neonate data was excluded (Table S1 row 5; r=−0.80, p<0.001, $R^2$=0.755).

The scatter plots of mean R2* values versus mean susceptibility values of all individual infant and adult subjects illustrate a significant positive linear correlation in DGM regions (blue regression line: $R2^*(\chi) = 0.731\ [ppb^{-1}\cdot s^{-1}]\ \chi + 4.09\ [s^{-1}]$, r=0.934, p<0.001, $R^2$=0.870) and a negative linear correlation in WM fiber bundles (black regression line:

$R2^*(\chi) = -0.535\ [ppb^{-1}\cdot s^{-1}]\cdot\chi + 5.76\ [s^{-1}]$, $r=-0.803$, $p<0.001$, $R^2=0.755$), as shown in Fig. S1.

### 3.2. Susceptibility in white matter

Regional magnetic susceptibilities were highly correlated with the microscopic myelin degree from the autopsy study (Brody, Kinney et al. 1987). Fig. 4 (a) illustrates the strong negative linear correlation found between myelination and bulk magnetic susceptibility ($r = -0.87$, $p < 0.005$, $R^2=0.832$). The linear regression yielded $\chi$ [ppm]= −0.0048 [ppm/degree] ∗ myelin [degree] −0.0048 [ppm].

Notably, there exists an outlier among the WM samples, which is presented via the magenta star in Fig. 4 (a). The autopsy study (Brody, Kinney et al. 1987) showed 0 degrees of myelination in neonatal BCC. However, the susceptibility value of neonatal BCC in this study is very negative ($\chi = -0.016 \pm 0.0061$ [ppm]) and almost equals to that of WM fibers with 2–3 degrees of myelination in 1-year-old BCC ($\chi = -0.015 \pm 0.0059$ [ppm]) and 2-year-old BCC ($\chi = -0.023 \pm 0.0093$ [ppm]) respectively. As shown in Fig. 4 (b), the corpus callosum in the neonate brain shows diamagnetic susceptibility, which is comparable to the corpus callosum at later ages (1 and 2-year-old).

Notably, the WM in the frontal lobe exhibits a paramagnetic susceptibility, while the susceptibility of WM in the temporal and occipital lobes is diamagnetic, as emphasized by the rectangular boxes in the top row of Fig. 5. The neonatal brain segmentation map is indicated in Fig. S2 in the supplemental material.

With increasing age, the magnetic susceptibility of WM in the neonate and infant brain evolves significantly as shown in Fig. 5. In the external capsule (EC, red dot arrows), the cortical spinal track (CST, magenta arrows) and posterior thalamic radiation (PTR, black arrows), we can observe a substantial increase in susceptibility contrast between WM and the surrounding GM. Although there is a low level of myelination in the neonatal brain, the susceptibility in the myelinated fibers (e.g. PLIC, CST and PTR) show clear diamagnetic contrast.

### 3.3. Susceptibility in Deep Gray Matter (DGM)

Fig. 6 shows the development of R2* and susceptibility in DGM nuclei at different ages. The mean susceptibility values in different DGM regions are presented in Table 1.

In the neonate R2* template (Fig. 6, top row of the left column), the boundaries between CN, PT and GP are smeared. In the 1-year and 2-year R2* templates, only CN shows lower contrast than PT and GP. It is difficult to visually distinguish PT, GP or even internal capsule (IC), which shows that R2* may not be suitable for detecting subtle iron deposition or myelination.

In the neonate QSM template (Fig. 6, bottom two rows of the left column), the susceptibility contrast of DGM nuclei compared to surrounding white matter (eg. PT, CN, and GP vs. IC and EC) is low. No clear boundaries between PT, CN and GP can be observed. The internal (GPi) and external (GPe) GP cannot be distinguished. All of the iron-rich nuclei show

negative susceptibility in the neonate brain (Table 1, left column). As the brain develops, the susceptibility contrast of the brain nuclei vs. its surroundings shows substantial and gradual increases. In the 1-year-old infant brains, the contrast between PT and EC, GP and IC, becomes much higher than that of the neonatal brain. This contrast keeps growing in the 2-year template, which clearly represents the elevated iron deposition and myelination process during this essential course of brain development. The structural boundaries between PT, CN and GP become clear, which demonstrates the asynchronous maturation among the DGM regions. In the 1-year and 2-year old brains, the GPi and GPe can be distinguished well based on susceptibility differences. Anatomically, the internal and external GP is physically separated by medial medullary lamina, which becomes thinner with human brain maturation, resulting in a blurred delineation between the two in the adult template. As presented in Table 1, from the neonates to adults, the susceptibility in each DGM nuclei shows continuous increase.

As denoted via the white dotted lines in the Fig. 6 top two rows, we extract the signals of QSM and R2* intensities in each age-specific template at that location. The intensity signals are then normalized ($s = \frac{s}{\text{norm}(s)}$, where s denotes the vectors of signal extracted from each template) for comparing purpose. For each age-group, the normalized intensity signals of R2* and QSM are plotted in the same profile line figure (Fig. 6 bottom two rows) to compare the contrast of the two different maps in presenting DGM nuclei structure. It is clear that from neonate to adult, in each age-group the profile lines for QSM denoted higher variations than the R2* profile lines, which quantitatively demonstrated that QSM provides better contrast in DGM region for distinguishing different brain nuclei.

### 3.4. Susceptibility in CSF

A comparison of susceptibility in CSF between neonates, infants and adults is shown in Fig. 7. The CSF regions are manually labelled in the T1w images and then propagated to the quantitative susceptibility maps. In the top row of Table 2, the mean susceptibility of CSF regions in the QSM template is provided. In the neonatal brains, the mean susceptibility in CSF is 58.0 ppb, this value decreases to 25.4 ppb for 1-year-old infants, 15.3 ppb for 2-year-old, and 6.4 ppb in the adult brains. Generally, the susceptibility in CSF shows gradually decreasing values with development of the neonate and infant brain and is much higher than in the adult brain. This observation suggests a more paramagnetic composition in the ventricles of neonate and infant brains.

## 4. Discussions

In the present work, we investigated susceptibility values in various brain structures in neonate and infant brains from birth to 2 years old. The basic characteristics between gray and white matters on the QSM images did not change through brain development from neonates to adults, i.e. gray matter tends to be paramagnetic while white matter tends to be diamagnetic. Our results led to several unique findings: 1) a linear regression was found between brain myelination in this study and microscopic myelin degree found by a previous autopsy study; 2) the brain myelinations in WM measured by QSM are region-specific, following a posterior-anterior spatial and temporal pattern; 3) iron continually accumulates

in deep gray matter from birth and a clear differentiation of the inner and outer GP can be revealed by QSM for 1-year and 2-year-old infants; 4) magnetic susceptibility values of CSF shows a gradually decreasing trend from birth to 2 years old and to adulthood. These structurally varying temporal characteristics may reflect different physiological processes: in the white matter, the characteristics are consistent with the myelination process; in the deep nuclei, the characteristics appear to be consistent with the changing iron deposits. These findings suggest that magnetic susceptibility directly reflects subtle variations in tissue composition through different ages in early brain development and may help us gain more insight into the potential abnormalities of magnetic susceptibility that arise from various neurological diseases.

### 4.1. Magnetic susceptibility and R2* development with age

As iron is the main contributor for R2* and susceptibility contrast elevation in human brain DGM regions. Using the exponential growth model, we are able to fit the R2* and susceptibility development with age in DGM through neonate, 1–2-year-old infant and adult brain. The iron-deposition in human brain accumulates fast in early age (0–20 year-old), this process slows down in the middle age (21–50 year-old) and the iron concentration slowly approximates saturation in the late age (>51 year-old) (Hallgren and Sourander 1958). In our study, the age gap between infant and adult is large, hence possibly induced bias in the fitted curves. Comparing with literatures (Hallgren and Sourander 1958, Li, Wu et al. 2014, Zhang, Wei et al. 2018), the fitted curve in our study denotes faster iron deposition process. Besides, the iron accumulates asynchronously in different DGM nucleus, in our study, the fitting curves are built using data from PT, GP and CN, thus the growth model presents the averaged iron deposition process from the three nuclei regions.

The WM fiber bundles presents a bi-directional development process through human life. In the early age, the neurons get myelination, which induce decrease in susceptibility and increase in R2*. The myelin content in WM achieves a peak around middles age of human, and degenerates in the late age (Lebel, Gee et al. 2012).

Although limited by the subject number and age gap, the regression curves shown in Fig. 3 demonstrated a consistent development trend in our study with previous works (Hallgren and Sourander 1958, Li, Wu et al. 2014, Zhang, Wei et al. 2018). The susceptibility in DGM and WM varies consistently with age and fitted smoothly with the growth models. Due to the inverted WM/GM contrast in neonate R2* map, the R2* development pattern in WM for neonate, 1–2-year-old infant shows inconsistent variation, the neonate R2* data is not modeled in the regression curves.

### 4.2. Correlation of R2* and magnetic susceptibility

Iron and myelin are two main contributors of both R2* and magnetic susceptibility contrast in vivo. R2* is a sum of relaxation due to spin-spin interaction (R2) and local susceptibility effects (R2’). R2’ and bulk susceptibility represent different measures of susceptibilities. While the bulk susceptibility can be considered as a volume average, R2’ represents the dephasing effect due to susceptibility variations in a volume, where diamagnetic and paramagnetic compounds hence the same effects. However, magnetic susceptibility can

distinguish paramagnetic iron from diamagnetic myelin, which are immediately discernible by magnetic susceptibility at opposite signs. Quantitative analysis of these two contrasts yields relative information about the underlying variation of iron and myelin, respectively (Table S1, Fig. S1).

Observed R2* changes are generally below those predicted by theory based a random, uniform distribution of ferritin particles. Several factors, e.g., clustering of particles or other types of ordering (alignment with fibers or preference for specific cellular compartments) may substantially alter R2*. This relevance for the quantification of tissue iron and myelin content form the joint analysis of R2* and magnetic susceptibility. Nevertheless, a linear relationship has been reported across GM of deep gray matter regions (Deistung, Schäfer et al. 2013). The positive correlation between R2* and susceptibility values in DGM are reported in literature (Deistung, Schäfer et al. 2013) based on in vivo adult brain data. Due to larger susceptibility range in adult brain tissue (Hallgren and Sourander 1958), the negative correlation between R2* and susceptibility values in WM is not well observed in this work. Our data covers more complete age-range than the previous study and thus lead to more precise regression analysis of the correlation between R2* and susceptibility. Notably when we excluded neonate and infant data and fit both WM and DGM VOIs from adult brain, the linear regression results is: $R2^*(\chi) = 0.249\ [ppb^{-1}\cdot s^{-1}]\ \chi + 44.86[s^{-1}]$, ($r=0.91$, $p<0.001$, $R^2=0.290$), which is similar to the result reported in the literature (Deistung, Schäfer et al. 2013): $R2^*(\chi) = 0.366\ [ppb^{-1}\cdot s^{-1}]\cdot\chi + 28.70[s^{-1}]$, ($r=0.93$, $p<0.001$, $R^2=0.870$). The slight differences on slope and offset of the regression lines are caused by strength field of scanner (7T versus 3T), and the reference regions of susceptibility (frontal deep white matter in literature and averaged susceptibility of whole brain in our study).

As indicated in magnified plots in Fig. S1, a large range of R2* was observed in neonate brain than those of infant age groups, while a smallest susceptibility was observed in the neonate brain. Considering the inverted WM-vs-GM R2* contrast between neonate and infant brain, we suspect the neonate brain data may involve bias in the regression analysis. Thus, after the neonate data was excluded, the strongest correlations can be observed as shown in Fig. S1 (black and blue lines).

### 4.3. GM-WM contrast in the neonate and infant brains

T1w and R2* images show a reversed contrast compared to the early-adult pattern (>12 months) (Fig. 2). This is caused by the incomplete myelination in the white matter and high water content of the neonatal brain. For example, the posterior limb of the internal capsule (PLIC) is one of the most myelinated regions at birth. Consequently, the signal intensity of the PLIC on T1w is significantly higher than other WM areas and also higher than that of the surrounding GM. The contrast of PLIC and its surrounding GM in neonate brain template is consistent with that in later age brain template. While for the same brain region in and R2* image, the signal intensity of PLIC is higher than the other WM areas and very close to that of the surrounding GM structures. The different contrast between T1w and R2* on PLIC and its surrounding GM structure is generally caused by (Barkovich, Kjos et al. 1988, van der Knaap and Valk 1990) the earlier presence of WM contrasts variation in T1w than in T2w (whereas R2* is derived). During the first year of postnatal life, the contrast

reversal in T1w is a biomarker of myelin maturation. However, after 1-year, T1w contrast does not change significantly. While the changes observed on T1w and R2* contrasts can be used to help understand maturation processes (Barkovich 2000, Prayer and Prayer 2003), T1w and T2w signals cannot be directly compared across individuals because of the variability between exams related to technical tunings (Dubois, Dehaene-Lambertz et al. 2014).

As a quantitative estimation of magnetic susceptibility of brain tissues, QSM provides consistent characteristics between gray and white matters throughout brain development from neonates to adults. Although there is a very low level of myelin in the neonatal brains, it shows diamagnetic susceptibility in the myelinated fiber bundles such as PLIC, PTR, CST and MCP. In the later ages, the regional susceptibility in WM bundles presented a gradually decreasing trend and is negatively correlated with the microscopic myelin degree (Fig. 4, Sec. 3.2). These findings underscored the significant effect of myelin on magnetic susceptibility in vivo, which is supported by previous studies that investigated the phase contrast of WM in the neonatal brains (Zhong, Ernst et al. 2011), as well as studies that compared susceptibility maps of transgenic shiverer mice (Liu, Li et al. 2011), and the study that examined mice on the cuprizone diet using T2* and phase images (Lee, Shmueli et al. 2012). As a potential approach for estimating myelin change (Stüber, Morawski et al. 2014), QSM provides improved and immediate observations on delicate myelin change in the *in-vivo* neonate and infant brain and is a promising means to assess the myelination process in a developing brain.

### 4.4. Contribution of iron and myelin for susceptibility in neonate and infant brains

Studies of the adult brain that used QSM have widely reported that iron and myelin provide the dominant source of susceptibility variations in DGM and WM respectively. In the neonate and infant brain, both iron storage and myelination are at low levels, and thus the contributions of iron and myelin for susceptibility are significantly reduced. Based on the region-specific observations in the neonate and infant brain, the dominant source of magnetic susceptibility in different brain region varies dramatically.

In the neonatal occipital lobe and temporal lobe, where myelination occurs earlier and evolves more quickly, WM exhibits a diamagnetic susceptibility. While in the frontal lobe, where myelination occurs later than birth, WM exhibits a paramagnetic susceptibility (Fig. 5, column 1, Sec. 3). The region-specific susceptibility in WM follows a posterior-anterior spatial pattern. This unique finding suggests that in the myelinated WM, the susceptibility is mostly dominated by myelin content. While in the unmyelinated WM, the dominant source of susceptibility is likely iron. Sufficient iron availability in the developing neonate and infant brain is essential to support neuronal and glial energy metabolism, dendritic arborization, synaptogenesis, neurotransmitter synthesis, and emerging myelination (Connor and Menzies 1996, Todorich, Pasquini et al. 2009). Studies of iron depositions in the neonatal rat brain suggested a highly localized distribution of ferritin-positive microglia and oligodendrocytes in WM (Connor, Pavlick et al. 1995, Cheepsunthorn, Palmer et al. 1998). Since no myelin is present in the neonatal frontal lobe, the major source of the paramagnetic susceptibility is likely due to the iron accumulating in microglia and oligodendrocytes. This

finding is also supported by studies that showed during the second post-natal week, the distribution of iron-positive oligodendrocytes co-localizes with the myelinogenic cell (Connor and Menzies 1996), while at the cellular level, iron-positive cells in the subventricular zone and myelinogenic foci are present as early as postnatal day 3 (Connor 1994).

On the other hand, the neonatal DGM exhibits a diamagnetic susceptibility (Table 1, column 1), which is another unique observation in the neonatal QSM template. In the post mortem study, Brody et al. reported myelin observations in the globus pallidus at birth (Brody, Kinney et al. 1987).

The essential role of QSM for determining iron distributions *in vivo* in the brain for aging and pathology studies has been widely discussed (Deistung, Schäfer et al. 2013, Li, Wu et al. 2014, Guan, Xuan et al. 2017). In adult (>30 year-old) GP, the non-haemin iron concentration is as high as 21.30 ± 3.49 mg/100g fresh tissue (Hallgren and Sourander 1958). A variety of MR contrasts, such as frequency, phase, and R2*, are able to investigate the iron deposition in the late age. However, in neonate and infant brains, the iron concentration is much lower (<2.5 mg/100g fresh tissue in globus pallidus & <1 mg/100g fresh tissue in putamen) (Hallgren and Sourander 1958). As shown in Fig. 6 (Sec. 3.2), although R2* is directly proportional to iron(Stüber, Morawski et al. 2014), it is not able to present the subtle iron deposits in neonate and infant brains. On the other hand, QSM provides unique high sensitivity for detecting the subtle variations (<1 mg/100g) of iron depositions in the early developmental DGM.

### 4.5. Contribution of macromolecules for susceptibility in neonate and infant brain CSF

In neonate and infant brains, the normal composition of CSF significantly differs from that of an adult brain. Reported by Ahmed et al. (Ahmed, Hickey et al. 1996, Seehusen, Reeves et al. 2003), normal CSF contains up to 20 White Blood Cells (WBC) per $mm^3$ in newborns and 5 White Blood Cells per $mm^3$ in adults. Besides, the CSF WBC count for neonates and infants also varies rapidly with age, as the CSF WBC count is significantly higher in neonates aged ≤28 days compared to neonates aged 29 to 56 days (Kestenbaum, Ebberson et al. 2010). Because the susceptibility of WBCs is more paramagnetic than water (Furlani 2007), the high WBC content in CSF in neonate brains may contribute to the high susceptibility in neonate CSF, and can also explain the gradual decrease of CSF susceptibility for neonate and 1–2 year-old infants.

On the other hand, the CSF protein concentrations are also higher in neonate and infant brains. The protein concentration shows a rapid fall from 1.08 g/L to 0.40 g/L within the first 6 months after birth (Biou, Benoist et al. 2000). A plateau (0.32 g/L) is reached from age 6 months to 10 years, followed by a slight increase (0.41 g/L) in the 10–16 years age range (Biou, Benoist et al. 2000). However, the susceptibility of these proteins is more diamagnetic than water (Furlani 2007). Together, this suggests that the susceptibility of WBC outweighs that of proteins, which contributes to the paramagnetic susceptibility in neonate and infant brains.

The paramagnetic susceptibility in neonatal CSF suggested that using CSF as the reference for susceptibility mapping is not suitable for neonatal studies. The high level of macromolecules in neonatal CSF may bring bias.

### 4.6 Contribution of axonal density and lipid for susceptibility in neonate brain

Previous work on baby brain development using diffusion tensor imaging (DTI) have demonstrated that most of the white matter structures seen in the adult brain with DTI have already been established in the neonatal brain. For example, Zhang et al. (Zhang, Evans et al. 2007) has shown that the major white matter fiber orientation did not change during first two years of life (Fig. 1 top row in (Zhang, Evans et al. 2007). Similar finding was reported by several studies based on the NIH MRI study of Normal Brain Development (http://www.brain-child.org/). While white matter anisotropy is relatively low in neonates and increases steadily with increasing age (Evans 2006). Regional anisotropy is thought to be influenced not only by myelination, but also by axon packing, the internal axonal structure, and the tissue water content (Hüppi and Dubois 2006). Thus, the susceptibility difference caused by susceptibility anisotropy among different age groups may be minor compared to that caused by white matter contents, i.e., axon density and myelination degree.

The axon in neonatal CC is denser than that in the later age (Partridge, Mukherjee et al. 2004). It is reported in the rhesus monkey, up to 70% of callosal axons are eliminated in the four first post-natal months (LaMantia and Rakic 1990). In humans, the number of axons in the CC may be close to a maximum in the newborn brain (with no new axons being formed to cross the midline), and the process of axonal pruning is supposed to occur after birth (Kostovic and Jovanov-Milosevic, 2006). Myelination is the last stage of WM development that begins after the process of axonal overproduction-pruning and follows pre-myelinating stages including the formation and maturation of oligodendrocytes (Thomas, Spassky et al. 2000). No myelin is presented in newborn brain CC (Brody, Kinney et al. 1987), and the myelination starts after 3 postnatal months in CC (Brody, Kinney et al. 1987), hence at birth, there is high possibility that the callosal axons are surrounded by immature oligodendrocytes. The immature oligodendrocytes are multipolar cells rich in a lipid called galactocerebroside (Miron, Kuhlmann et al. 2011) and account for 30–40% of the entire oligodendroglia population in the preterm period (28–37 w GA) (Morell and Quarles 2011).Therefore, we may infer that these lipid content induced the diamagnetic susceptibility in neonate CC, plus the super dense pack of the callosal axons, these two factors significantly contribute to the outstanding negative bulk susceptibility in neonate CC.

A peak of myelination is observed during the first post-natal year. In 1-year-old infant brain, the myelin content in CC is still low, for providing nutrition (iron is one of the most importance compartment) to myelination, the mature oligodendrocytes around axons induced paramagnetic susceptibility. With the process of axonal pruning, the axon density at 1-year-old is lower than that at birth. Therefore, although myelinated, the susceptibility observed in 1-year-old CC is almost equal to that observed in neonate CC (Fig. 4 (a)). In 2-year-old brain, the myelin content in CC becomes higher, hence the susceptibility we observed is more diamagnetic than in neonate and 1-year-old CC.

### 4.7 Limitations

QSM and R2* mapping have been identified and validated as the most promising approaches for iron mapping in the brain deep gray matter regions. White matter has a diamagnetic bulk susceptibility which is mainly constituted by the myelin and tissue water which means that the paramagnetic effect of iron is counteracted by the diamagnetic myelin (He and Yablonskiy 2009, Fukunaga, Li et al. 2010). Previous study on the separation of iron content of the white matter based on the temperature dependency of the paramagnetic effect of iron (Christoph, Christian et al. 2015). However, it is clearly not possible to change brain temperature in vivo, therefore, the clinical applicability of this method to separate the iron and myelin remain limited. Recently, Lee et al (Lee, Nam et al. 2017) proposed a new QSM algorithm to separates positive and negative susceptibility sources within a voxel by utilizing signal relaxation (R2`) for dipole inversion. However, its application is still under investigation.

In the present study, the subject number across age is evenly distributed. However, the number is limited due to the specific early age. The number of neonate and infant subjects is very limited, and many motion-corrupted data are excluded. The strategy of building age-specific template overcomes the bias related to age, but the lack of young participants caused a few gaps (e.g. 3-6-9-months-old infant) for further specializing age groups. The contrast between WM and GM totally inverted in R2* images for neonate comparing with 1-year-old brain, the undergoing mechanism of brain maturation process that related to R2* contrast variation could be presented in the 3-6-9-months-old infant brains.

For QSM reconstruction, we employed the whole brain average susceptibility as reference. For testing the assumption that “all subjects have similar average whole brain mean susceptibility” is true for each age-group, we computed the average of whole brain susceptibility for all the subjects with different ages and then collected the mean and S.D. of each specific age-group as shown in the Table S2 in the supplementary material. The mean susceptibility for whole brain at each age-group are close to zero (around $10^{-2}$ ppb for neonate and infant brain; and around $10^{-1}$ ppb for adult brain). In literatures, CSF, frontal deep WM and occipital WM are common regions chosen as reference region for adult brain QSM computation (Langkammer, Krebs et al. 2012, Deistung, Schäfer et al. 2013). Using the JHU atlas for neonate and infant brain region segmentation, as well home-made QSM atlas (Zhang, Wei et al. 2018, Zhang, Wei et al. 2018) for adult brain segmentation, we computed the mean and S.D. of susceptibility of these common reference regions, and presented in Table S2 bottom rows. Comparing with the susceptibility value in bottom three rows, using “whole brain average susceptibility” as reference is demonstrated as the best choice for the data used in this study.

## 5. Conclusion.

In the present work, we investigated susceptibility values in various brain structures in neonate and infant brains from birth to 2 years old. Based on the consistent characteristics between gray and white matters along brain development, QSM provided unique findings in WM, DGM nuclei and CSF, which demonstrates its ability to present subtle variations in tissue composition through different ages in early brain development. QSM can be a means

to study early brain development and related pathologies that involve alterations in myelin, iron and macromolecular content.

## Supplementary Material

Refer to Web version on PubMed Central for supplementary material.

## References


Ahmed A, Hickey SM, Ehrett S, Trujillo M, Brito F, Goto C, Olsen K, Krisher K and McCracken GH, Jr (1996). "Cerebrospinal fluid values in the term neonate." The Pediatric infectious disease journal 15(4): 298–303. [PubMed: 8866797]

Barkovich AJ (2000). "Concepts of Myelin and Myelination in Neuroradiology." American Journal of Neuroradiology 21(6): 1099–1109. [PubMed: 10871022]

Barkovich AJ, Kjos BO, D E Jackson J and Norman D (1988). "Normal maturation of the neonatal and infant brain: MR imaging at 1.5 T." Radiology 166(1): 173–180. [PubMed: 3336675]

Beaulieu C (2002). "The basis of anisotropic water diffusion in the nervous system – a technical review." NMR in Biomedicine 15(7–8): 435–455. [PubMed: 12489094]

Bingham NH and Fry JM (2010). Adding additional covariates and the analysis of covariance Regression: Linear Models in Statistics. London, Springer: 129–148.

Biou D, Benoist J-F, Nguyen-Thi C, Huong X, Morel P and Marchand M (2000). "Cerebrospinal fluid protein concentrations in children: age-related values in patients without disorders of the central nervous system." Clinical chemistry 46(3): 399–403. [PubMed: 10702528]

Brody BA, Kinney HC, Kloman AS and Gilles FH (1987). "Sequence of central nervous system myelination in human infancy. I. An autopsy study of myelination." Journal of Neuropathology & Experimental Neurology 46(3): 283–301. [PubMed: 3559630]

Carpenter KL, Li W, Wei H, Wu B, Xiao X, Liu C, Worley G and Egger HL (2016). "Magnetic susceptibility of brain iron is associated with childhood spatial IQ." NeuroImage 132: 167–174. [PubMed: 26899787]

Cheepsunthorn P, Palmer C and Connor JR (1998). "Cellular distribution of ferritin subunits in postnatal rat brain." Journal of Comparative Neurology 400(1): 73–86. [PubMed: 9762867]

Christoph B, Christian L, Heinz K, Walter G, Christina E, Johannes H, Rudolf S, Franz F and Stefan R (2015). "Iron mapping using the temperature dependency of the magnetic susceptibility." Magnetic Resonance in Medicine 73(3): 1282–1288. [PubMed: 24752873]

Connor JR (1994). "Iron acquisition and expression of iron regulatory proteins in the developing brain: manipulation by ethanol exposure, iron deprivation and cellular dysfunction." Developmental neuroscience 16(5–6): 233–247. [PubMed: 7768202]

Connor JR and Menzies SL (1996). "Relationship of iron to oligondendrocytes and myelination." Glia 17(2): 83–93. [PubMed: 8776576]

Connor JR, Pavlick G, Karli D, Menzies SL and Palmer C (1995). "A histochemical study of iron-positive cells in the developing rat brain." Journal of Comparative Neurology 355(1): 111–123. [PubMed: 7636007]

Cronin MJ, Wang N, Decker KS, Wei H, Zhu W-Z and Liu C (2017). "Exploring the origins of echo-time-dependent quantitative susceptibility mapping (QSM) measurements in healthy tissue and cerebral microbleeds." NeuroImage 149: 98–113. [PubMed: 28126551]

de Rochefort L, Liu T, Kressler B, Liu J, Spincemaille P, Lebon V, Wu J and Wang Y (2010). "Quantitative susceptibility map reconstruction from MR phase data using bayesian regularization: validation and application to brain imaging." Magnetic Resonance in Medicine 63(1): 194–206. [PubMed: 19953507]

Deistung A, Rauscher A, Sedlacik J, Stadler J, Witoszynskyj S and Reichenbach JR (2008). "Susceptibility weighted imaging at ultra high magnetic field strengths: theoretical considerations and experimental results." Magnetic Resonance in Medicine 60(5): 1155–1168. [PubMed: 18956467]

Deistung A, Schäfer A, Schweser F, Biedermann U, Turner R and Reichenbach JR (2013). “Toward in vivo histology: a comparison of quantitative susceptibility mapping (QSM) with magnitude-, phase-, and R 2∗-imaging at ultra-high magnetic field strength.” Neuroimage 65: 299–314. [PubMed: 23036448]

Deoni SC, Mercure E, Blasi A, Gasston D, Thomson A, Johnson M, Williams SC and Murphy DG (2011). “Mapping infant brain myelination with magnetic resonance imaging.” Journal of Neuroscience 31(2): 784–791. [PubMed: 21228187]

Deoni SCL, Dean DC, O’Muircheartaigh J, Dirks H and Jerskey BA (2012). “Investigating white matter development in infancy and early childhood using myelin water faction and relaxation time mapping.” NeuroImage 63(3): 1038–1053. [PubMed: 22884937]

Deoni SCL, Matthews L and Kolind SH (2013). “One component? Two components? Three? The effect of including a nonexchanging “free” water component in multicomponent driven equilibrium single pulse observation of T1 and T2.” Magnetic Resonance in Medicine 70(1): 147–154. [PubMed: 22915316]

Dibb R, Xie L, Wei H and Liu C (2017). “Magnetic susceptibility anisotropy outside the central nervous system.” NMR in Biomedicine 30(4).

Dubois J, Dehaene-Lambertz G, Kulikova S, Poupon C, Hüppi PS and Hertz-Pannier L (2014). “The early development of brain white matter: a review of imaging studies in fetuses, newborns and infants.” Neuroscience 276: 48–71. [PubMed: 24378955]

Dubois J, Dehaene-Lambertz G, Perrin M, Mangin JF, Cointepas Y, Duchesnay E, Le Bihan D and Hertz-Pannier L (2008). “Asynchrony of the early maturation of white matter bundles in healthy infants: quantitative landmarks revealed noninvasively by diffusion tensor imaging.” Human brain mapping 29(1): 14–27. [PubMed: 17318834]

Evans AC (2006). “The NIH MRI study of normal brain development.” NeuroImage 30(1): 184–202. [PubMed: 16376577]

Fukunaga M, Li T-Q, van Gelderen P, de Zwart JA, Shmueli K, Yao B, Lee J, Maric D, Aronova MA, Zhang G, Leapman RD, Schenck JF, Merkle H and Duyn JH (2010). “Layer-specific variation of iron content in cerebral cortex as a source of MRI contrast.” Proceedings of the National Academy of Sciences 107(8): 3834–3839.

Furlani E (2007). “Magnetophoretic separation of blood cells at the microscale.” Journal of Physics D: Applied Physics 40(5): 1313.

Gilmore JH, Lin W, Corouge I, Vetsa Y, Smith JK, Kang C, Gu H, Hamer R, Lieberman J and Gerig G (2007). “Early postnatal development of corpus callosum and corticospinal white matter assessed with quantitative tractography.” American Journal of Neuroradiology 28(9): 1789–1795. [PubMed: 17923457]

Guan X, Xuan M, Gu Q, Huang P, Liu C, Wang N, Xu X, Luo W and Zhang M (2017). “Regionally progressive accumulation of iron in Parkinson’s disease as measured by quantitative susceptibility mapping.” NMR in Biomedicine 30(4).

Hüppi PS and Dubois J (2006). “Diffusion tensor imaging of brain development.” Seminars in Fetal and Neonatal Medicine 11(6): 489–497. [PubMed: 16962837]

Haacke EM, Miao Y, Liu M, Habib CA, Katkuri Y, Liu T, Yang Z, Lang Z, Hu J and Wu J (2010). “Correlation of putative iron content as represented by changes in R2* and phase with age in deep gray matter of healthy adults.” Journal of Magnetic Resonance Imaging 32(3): 561–576. [PubMed: 20815053]

Hallgren B and Sourander P (1958). “The effect of age on the non-haemin iron in the human brain.” Journal of neurochemistry 3(1): 41–51. [PubMed: 13611557]

He X and Yablonskiy DA (2009). “Biophysical mechanisms of phase contrast in gradient echo MRI.” Proceedings of the National Academy of Sciences 106(32): 13558–13563.

Huang H, Zhang J, Wakana S, Zhang W, Ren T, Richards LJ, Yarowsky P, Donohue P, Graham E and van Zijl PC (2006). “White and gray matter development in human fetal, newborn and pediatric brains.” Neuroimage 33(1): 27–38. [PubMed: 16905335]

Jones DK, Knösche TR and Turner R (2013). “White matter integrity, fiber count, and other fallacies: The do’s and don’ts of diffusion MRI.” NeuroImage 73: 239–254. [PubMed: 22846632]

J. D. K and Mara C (2010). “Twenty-five pitfalls in the analysis of diffusion MRI data.” NMR in Biomedicine 23(7): 803–820. [PubMed: 20886566]

Kestenbaum LA, Ebberson J, Zorc JJ, Hodinka RL and Shah SS (2010). “Defining cerebrospinal fluid white blood cell count reference values in neonates and young infants.” Pediatrics 125(2): 257–264. [PubMed: 20064869]

Kinney HC, Brody BA, Kloman AS and Gilles FH (1988). “Sequence of central nervous system myelination in human infancy: II. Patterns of myelination in autopsied infants.” Journal of Neuropathology & Experimental Neurology 47(3): 217–234. [PubMed: 3367155]

Knickmeyer RC, Gouttard S, Kang C, Evans D, Wilber K, Smith JK, Hamer RM, Lin W, Gerig G and Gilmore JH (2008). “A structural MRI study of human brain development from birth to 2 years.” Journal of Neuroscience 28(47): 12176–12182. [PubMed: 19020011]

Kolasinski J, Takahashi E, Stevens AA, Benner T, Fischl B, Zöllei L and Grant PE (2013). “Radial and tangential neuronal migration pathways in the human fetal brain: anatomically distinct patterns of diffusion MRI coherence.” Neuroimage 79: 412–422. [PubMed: 23672769]

Krystek M and Anton M (2008). “A weighted total least-squares algorithm for fitting a straight line.” Measurement Science and Technology 19(7): 079801.

LaMantia A and Rakic P (1990). “Axon overproduction and elimination in the corpus callosum of the developing rhesus monkey.” The Journal of Neuroscience 10(7): 2156–2175. [PubMed: 2376772]

Langkammer C, Krebs N, Goessler W, Scheurer E, Yen K, Fazekas F and Ropele S (2012). “Susceptibility induced gray–white matter MRI contrast in the human brain.” Neuroimage 59(2): 1413–1419. [PubMed: 21893208]

Lebel C, Gee M, Camicioli R, Wieler M, Martin W and Beaulieu C (2012). “Diffusion tensor imaging of white matter tract evolution over the lifespan.” Neuroimage 60(1): 340–352. [PubMed: 22178809]

Lee J, Nam Y, Choi JY, Shin H, Hwang T and Lee J (2017). Separating positive and negative susceptibility sources in QSM. ISMRM, HONOLULU,HI,USA, MRM.

Lee J, Shmueli K, Kang B-T, Yao B, Fukunaga M, Van Gelderen P, Palumbo S, Bosetti F, Silva AC and Duyn JH (2012). “The contribution of myelin to magnetic susceptibility-weighted contrasts in high-field MRI of the brain.” Neuroimage 59(4): 3967–3975. [PubMed: 22056461]

Li W, Wu B, Batrachenko A, Bancroft-Wu V, Morey RA, Shashi V, Langkammer C, Bellis MD, Ropele S and Song AW (2014). “Differential developmental trajectories of magnetic susceptibility in human brain gray and white matter over the lifespan.” Human brain mapping 35(6): 2698–2713. [PubMed: 24038837]

Liu C (2010). “Susceptibility tensor imaging.” Magnetic resonance in medicine 63(6): 1471–1477. [PubMed: 20512849]

Liu C, Li W, Johnson GA and Wu B (2011). “High-field (9.4 T) MRI of brain dysmyelination by quantitative mapping of magnetic susceptibility.” Neuroimage 56(3): 930–938. [PubMed: 21320606]

Liu C, Li W, Wu B, Jiang Y and Johnson GA (2012). “3D fiber tractography with susceptibility tensor imaging.” Neuroimage 59(2): 1290–1298. [PubMed: 21867759]

Miron VE, Kuhlmann T and Antel JP (2011). “Cells of the oligodendroglial lineage, myelination, and remyelination.” Biochimica et Biophysica Acta (BBA) - Molecular Basis of Disease 1812(2): 184–193. [PubMed: 20887785]

Morell P and Quarles RB (2011). “Characteristic Composition of Myelin.” Journal of Neuroscience 31(2): 784–791. [PubMed: 21228187]

Oishi K, Mori S, Donohue PK, Ernst T, Anderson L, Buchthal S, Faria A, Jiang H, Li X and Miller MI (2011). “Multi-contrast human neonatal brain atlas: application to normal neonate development analysis.” Neuroimage 56(1): 8–20. [PubMed: 21276861]

Partridge SC, Mukherjee P, Henry RG, Miller SP, Berman JI, Jin H, Lu Y, Glenn OA, Ferriero DM and Barkovich AJ (2004). “Diffusion tensor imaging: serial quantitation of white matter tract maturity in premature newborns.” Neuroimage 22(3): 1302–1314. [PubMed: 15219602]

Prayer D and Prayer L (2003). “Diffusion-weighted magnetic resonance imaging of cerebral white matter development.” European Journal of Radiology 45(3): 235–243. [PubMed: 12595108]

Qiu A, Mori S and Miller MI (2015). “Diffusion tensor imaging for understanding brain development in early life.” Annual review of psychology 66: 853–876.

Schofield MA and Zhu Y (2003). “Fast phase unwrapping algorithm for interferometric applications.” Optics letters 28(14): 1194–1196. [PubMed: 12885018]

Schweser F, Deistung A, Lehr BW and Reichenbach JR (2011). “Quantitative imaging of intrinsic magnetic tissue properties using MRI signal phase: an approach to in vivo brain iron metabolism?” Neuroimage 54(4): 2789–2807. [PubMed: 21040794]

Seehusen DA, Reeves MM and Fomin D (2003). “Cerebrospinal fluid analysis.” American family physician 68(6): 1103–1108. [PubMed: 14524396]

Shmueli K, de Zwart JA, van Gelderen P, Li TQ, Dodd SJ and Duyn JH (2009). “Magnetic susceptibility mapping of brain tissue in vivo using MRI phase data.” Magnetic resonance in medicine 62(6): 1510–1522. [PubMed: 19859937]

Smith SM, Jenkinson M, Woolrich MW, Beckmann CF, Behrens TE, Johansen-Berg H, Bannister PR, De Luca M, Drobnjak I and Flitney DE (2004). “Advances in functional and structural MR image analysis and implementation as FSL.” Neuroimage 23: S208–S219. [PubMed: 15501092]

Spong CY (2013). “Defining “term” pregnancy: recommendations from the Defining “Term” Pregnancy Workgroup.” Jama 309(23): 2445–2446. [PubMed: 23645117]

Stüber C, Morawski M, Schäfer A, Labadie C, Wähnert M, Leuze C, Streicher M, Barapatre N, Reimann K, Geyer S, Spemann D and Turner R (2014). “Myelin and iron concentration in the human brain: A quantitative study of MRI contrast.” NeuroImage 93: 95–106. [PubMed: 24607447]

Thomas J-L, Spassky N, Perez Villegas EM, Olivier C, Cobos I, Goujet-Zalc C, Martínez S and Zalc B (2000). “Spatiotemporal development of oligodendrocytes in the embryonic brain.” Journal of Neuroscience Research 59(4): 471–476. [PubMed: 10679785]

Todorich B, Pasquini JM, Garcia CI, Paez PM and Connor JR (2009). “Oligodendrocytes and myelination: the role of iron.” Glia 57(5): 467–478. [PubMed: 18837051]

van der Knaap MS and Valk J (1990). “MR imaging of the various stages of normal myelination during the first year of life.” Neuroradiology 31(6): 459–470. [PubMed: 2352626]

Vercauteren T, Pennec X, Perchant A and Ayache N (2009). “Diffeomorphic demons: Efficient non-parametric image registration.” NeuroImage 45(1): S61–S72. [PubMed: 19041946]

Wei H, Dibb R, Decker K, Wang N, Zhang Y, Zong X, Lin W, Nissman DB and Liu C (2017). “Investigating magnetic susceptibility of human knee joint at 7 tesla.” Magnetic Resonance in Medicine.

Wei H, Dibb R, Zhou Y, Sun Y, Xu J, Wang N and Liu C (2015). “Streaking artifact reduction for quantitative susceptibility mapping of sources with large dynamic range.” NMR in Biomedicine 28(10): 1294–1303. [PubMed: 26313885]

Wei H, Gibbs E, Zhao P, Wang N, Cofer GP, Zhang Y, Johnson GA and Liu C (2017). “Susceptibility tensor imaging and tractography of collagen fibrils in the articular cartilage.” Magnetic resonance in medicine 78(5): 1683–1690. [PubMed: 28856712]

Wei H, Xie L, Dibb R, Li W, Decker K, Zhang Y, Johnson GA and Liu C (2016). “Imaging whole-brain cytoarchitecture of mouse with MRI-based quantitative susceptibility mapping.” NeuroImage 137: 107–115. [PubMed: 27181764]

Wei H, Zhang Y, Gibbs E, Chen NK, Wang N and Liu C (2016). “Joint 2D and 3D phase processing for quantitative susceptibility mapping: application to 2D echo-planar imaging.” NMR in Biomedicine.

Wharton S, Schäfer A and Bowtell R (2010). “Susceptibility mapping in the human brain using threshold-based k-space division.” Magnetic resonance in medicine 63(5): 1292–1304. [PubMed: 20432300]

Wu B, Li W, Guidon A and Liu C (2012). “Whole brain susceptibility mapping using compressed sensing.” Magnetic resonance in medicine 67(1): 137–147. [PubMed: 21671269]

Wu G, Jia H, Wang Q and Shen D (2010). “Groupwise registration with sharp mean.” Medical Image Computing and Computer-Assisted Intervention–MICCAI 2010: 570–577.

Wu G, Jia H, Wang Q and Shen D (2011). “SharpMean: groupwise registration guided by sharp mean image and tree-based registration.” NeuroImage 56(4): 1968–1981. [PubMed: 21440646]

Zhang J, Evans A, Hermoye L, Lee S-K, Wakana S, Zhang W, Donohue P, Miller MI, Huang H, Wang X, van Zijl PCM and Mori S (2007). "Evidence of slow maturation of the superior longitudinal fasciculus in early childhood by diffusion tensor imaging." NeuroImage 38(2): 239–247. [PubMed: 17826183]

Zhang Y, Shi F, Wu G, Wang L, Yap P-T and Shen D (2016). "Consistent spatial-temporal longitudinal atlas construction for developing infant brains." IEEE transactions on medical imaging 35(12): 2568–2577. [PubMed: 27392345]

Zhang Y, Shi F, Yap PT and Shen D (2016). "Detail-preserving construction of neonatal brain atlases in space-frequency domain." Human brain mapping 37(6): 2133–2150. [PubMed: 26987787]

Zhang Y, Wei H, Cronin MJ, He N, Yan F and Liu C (2018). "Longitudinal atlas for normative human brain development and aging over the lifespan using quantitative susceptibility mapping." NeuroImage.

Zhang Y, Wei H, Cronin MJ, He N, Yan F and Liu C (2018). "Longitudinal atlas for normative human brain development and aging over the lifespan using quantitative susceptibility mapping." NeuroImage 171: 176–189. [PubMed: 29325780]

Zhang Y, Wei H, Cronin MJ, He N, Yan F and Liu C (2018). "Longitudinal data for magnetic susceptibility of normative human brain development and aging over the lifespan." Data in Brief.

Zhong K, Ernst T, Buchthal S, Speck O, Anderson L and Chang L (2011). "Phase contrast imaging in neonates." Neuroimage 55(3): 1068–1072. [PubMed: 21232619]

**Specific statement in this paper:**

**Neonate:**

presents the newborns.

**Infant:**

presents the 1-year-old and 2-year-old infants.

**Myelination:**

myelin formation around axons.

**Axon pruning:**

a strategy often used to selectively remove exuberant neuronal branches and connections in the immature nervous system to ensure the proper formation of functional circuitry.

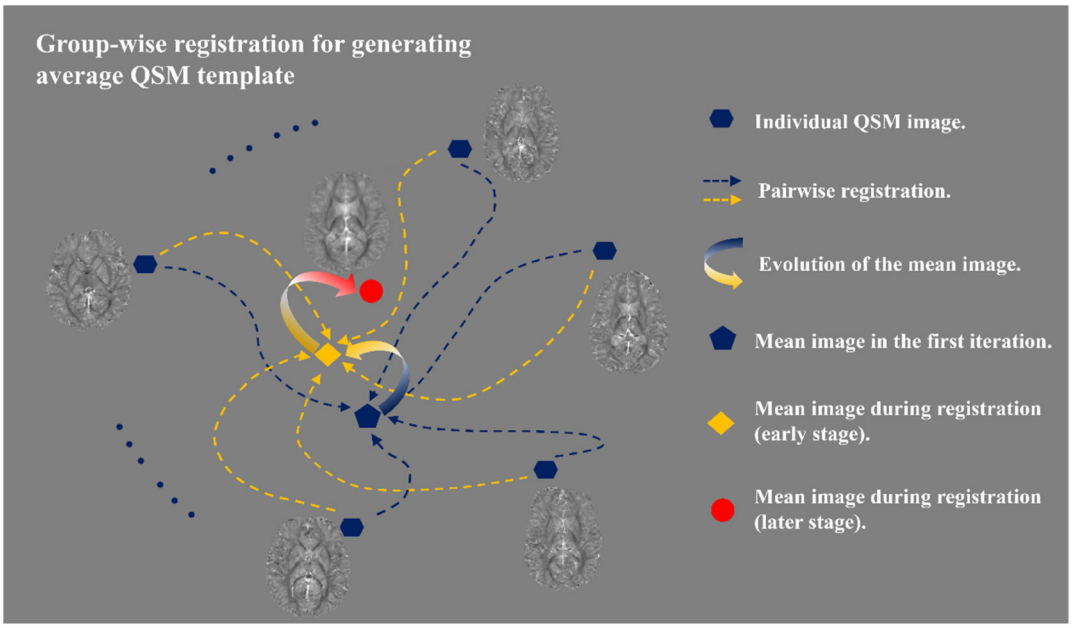


**Figure 1. Group-wise registration for average QSM template construction.**

For each age-specific group, individual susceptibility maps (denoted by blue hexagons) are combined as in eq. (1) to generate the template susceptibility map (denoted by red circular) iteratively. Each loop refines the QSM template.

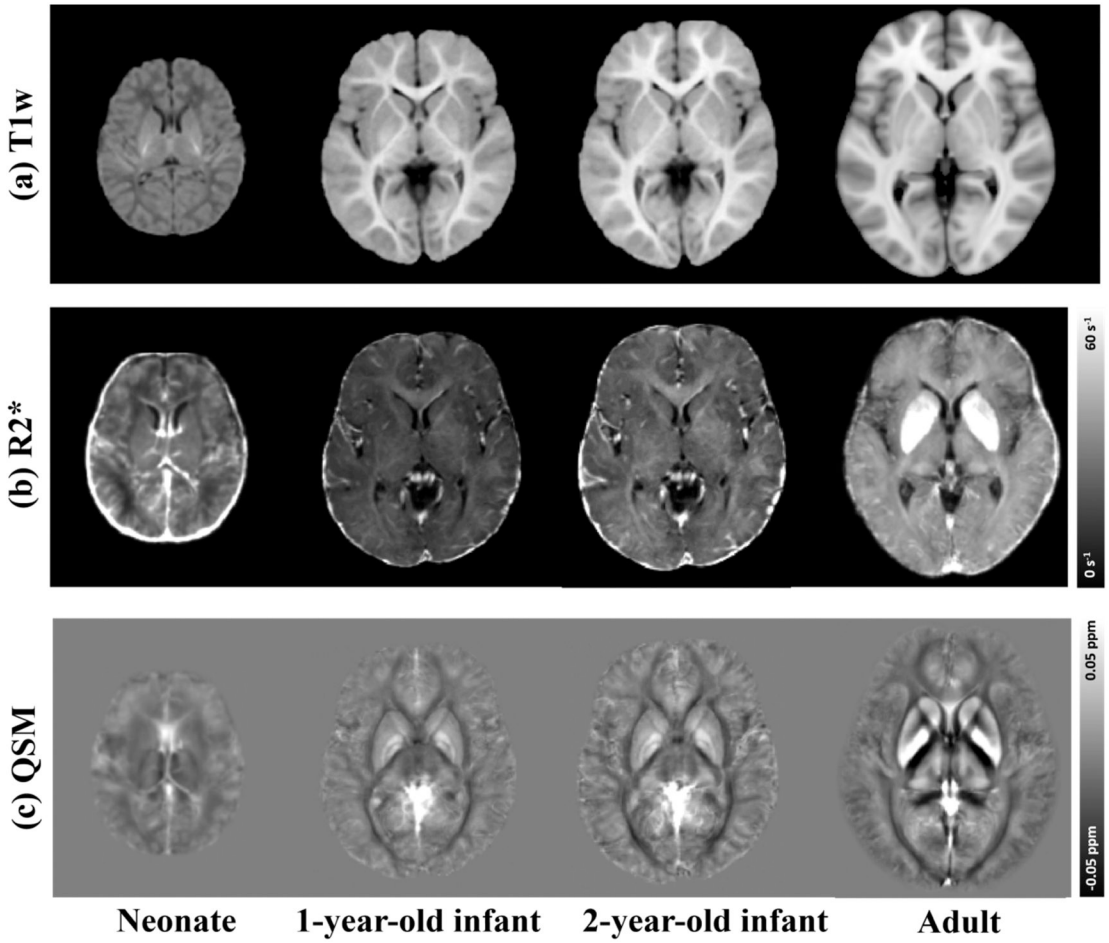


**Figure 2.**

Comparison of (a) T1w templates, (b) R2* templates and (c) susceptibility map templates for neonates, 1-year-old infants, 2-year-old infants and adults.

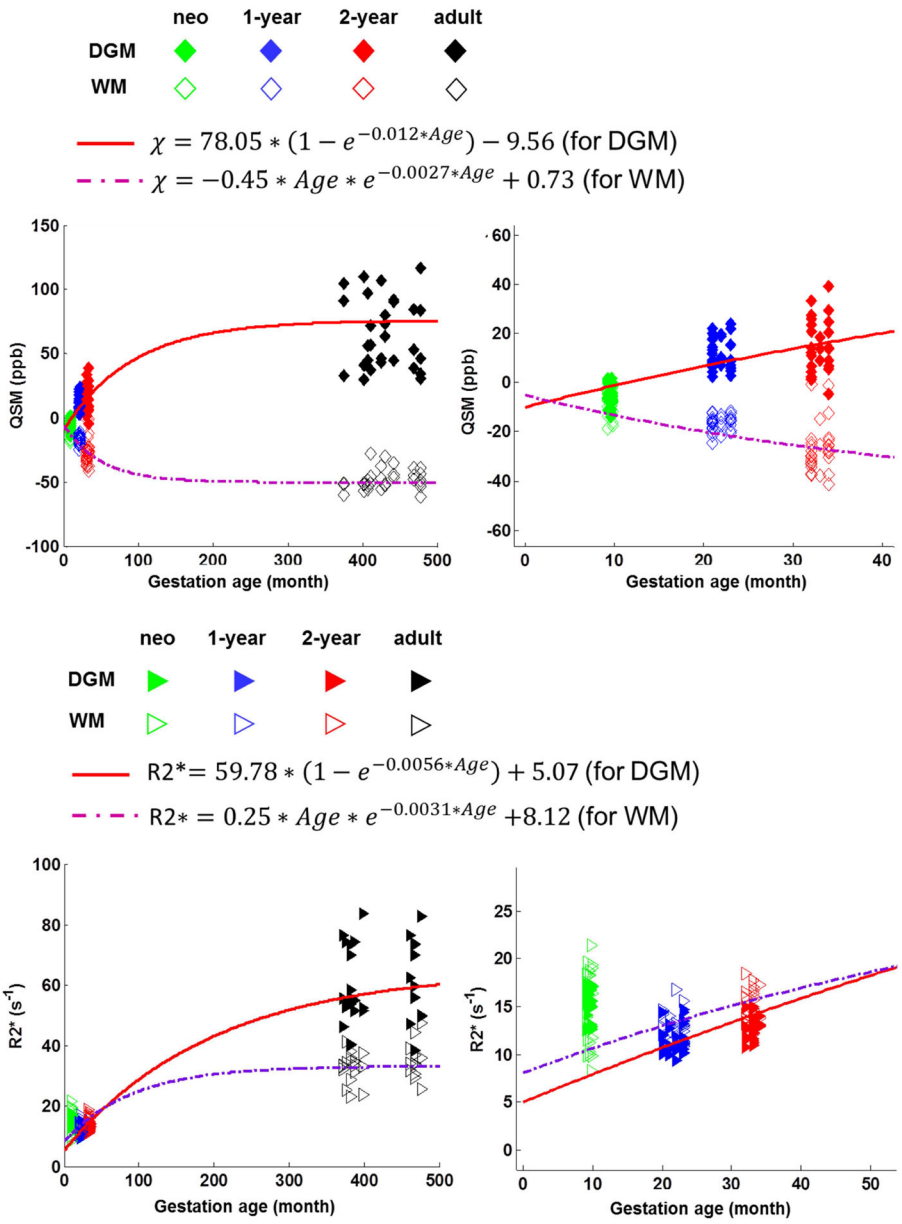


**Figure 3. Regression analysis indicating susceptibility χ [ppb] and R2* [$s^{-1}$] development pattern with age in neonate, infant and adult brains.**

The magnetic susceptibility curves in DGM (red line) and WM (purple dotted line) regions are plotted as a function of monthly gestation age respectively (top row). The R2* relaxation rate in DGM (red line) and WM (purple dotted line) regions are plotted as a function of monthly gestation age respectively (bottom row).

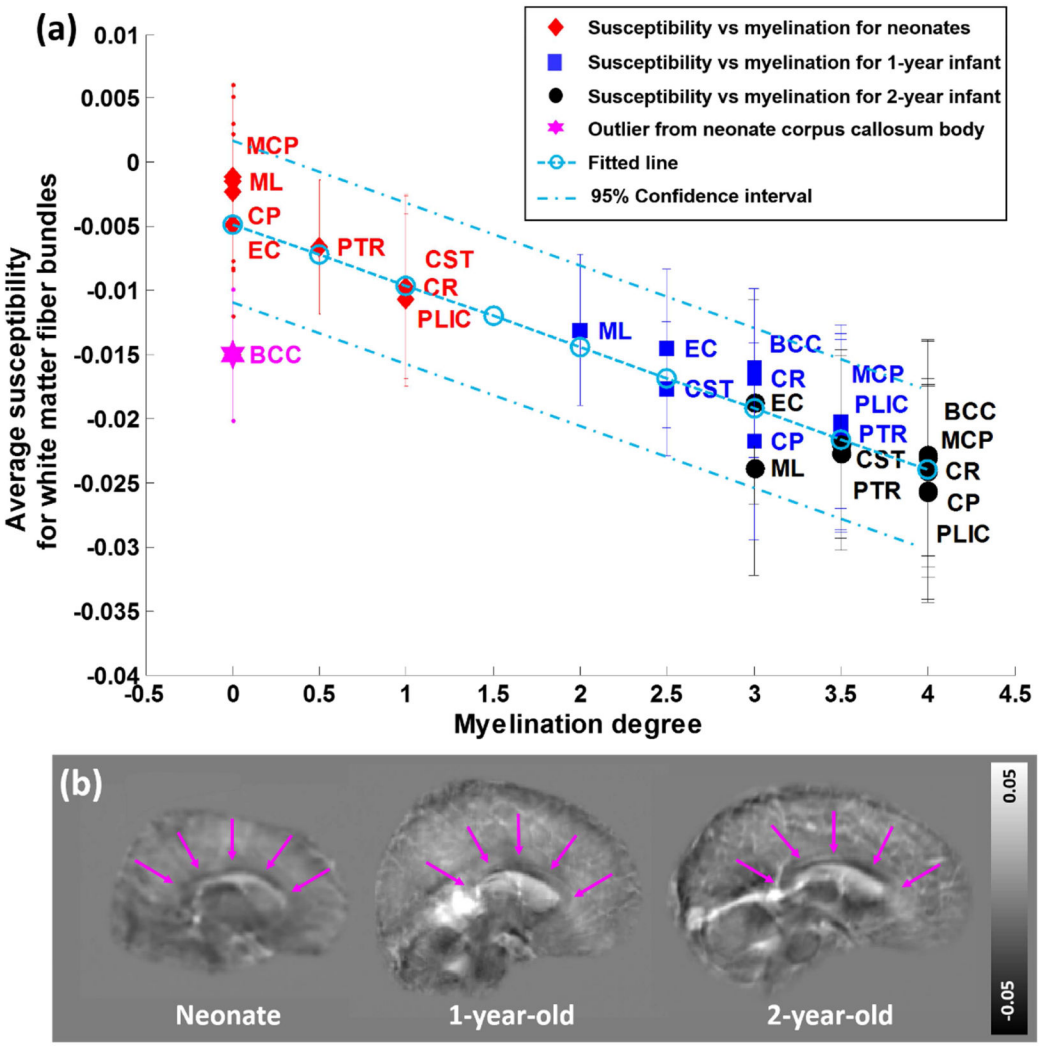


**Figure 4. Susceptibility development correlated with myelination degree in white matter fiber bundles for neonates and infants up to 2 years old. (a) Linear regression line indicating susceptibility vs myelination degree. (b) Susceptibility evolution in corpus callosum.**

The purple arrows pointed to the CC region for each age-specific template. Abbreviations: BCC, body corpus callosum; SCC, splenium corpus callosum; EC, external capsule; MCP, middle cerebellar peduncle; PTR, posterior thalamic radiation; CR, corona radiata; PCT, pontine crossing tract; ML, medial lemniscus; CST, corticospinal tract; PLIC, posterior limb of internal capsule; CP: cerebral peduncle.

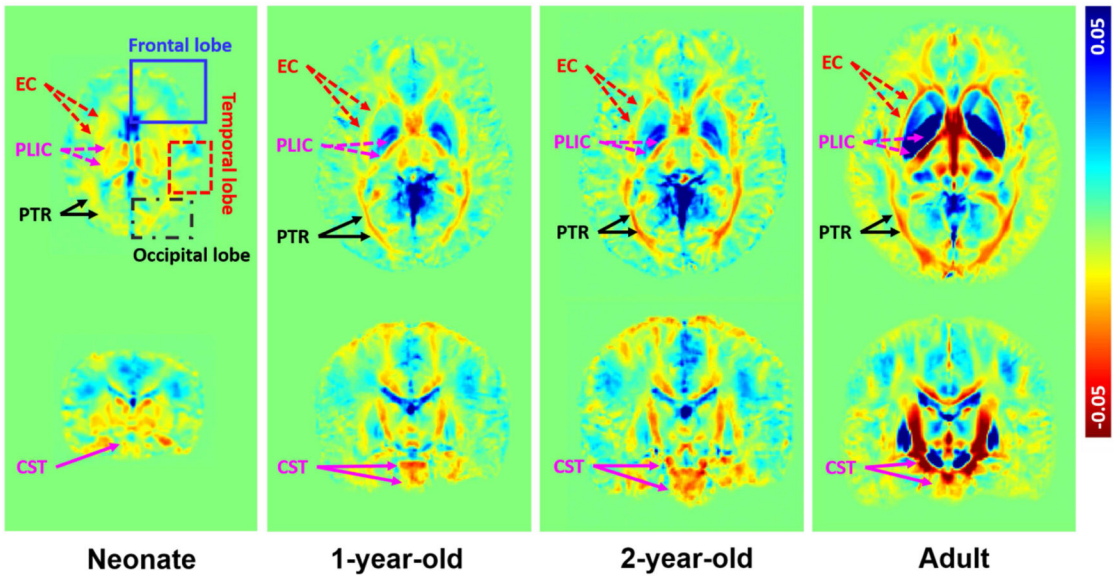


**Figure 5. Comparison of QSM color-coded maps for neonates, 1-year-old infants, 2-year-old infants and adults.**

First row: the axial section. The rectangular box in the neonatal brain presents the paramagnetic susceptibility in the frontal lobe white matter; the dotted-line rectangular boxes indicate the diamagnetic susceptibility in the temporal lobe and occipital lobe white matter. The neonatal brain segmentation map is indicated in Fig. S2 in the supplemental material. The black arrows indicate posterior thalamic radiation (PTR), the magenta dotted arrows show the posterior limb of internal capsule (PLIC), and the red dotted arrows point to the external capsule (EC). Bottom row: the coronal section. The magenta arrows show the cortical spinal track (CST).

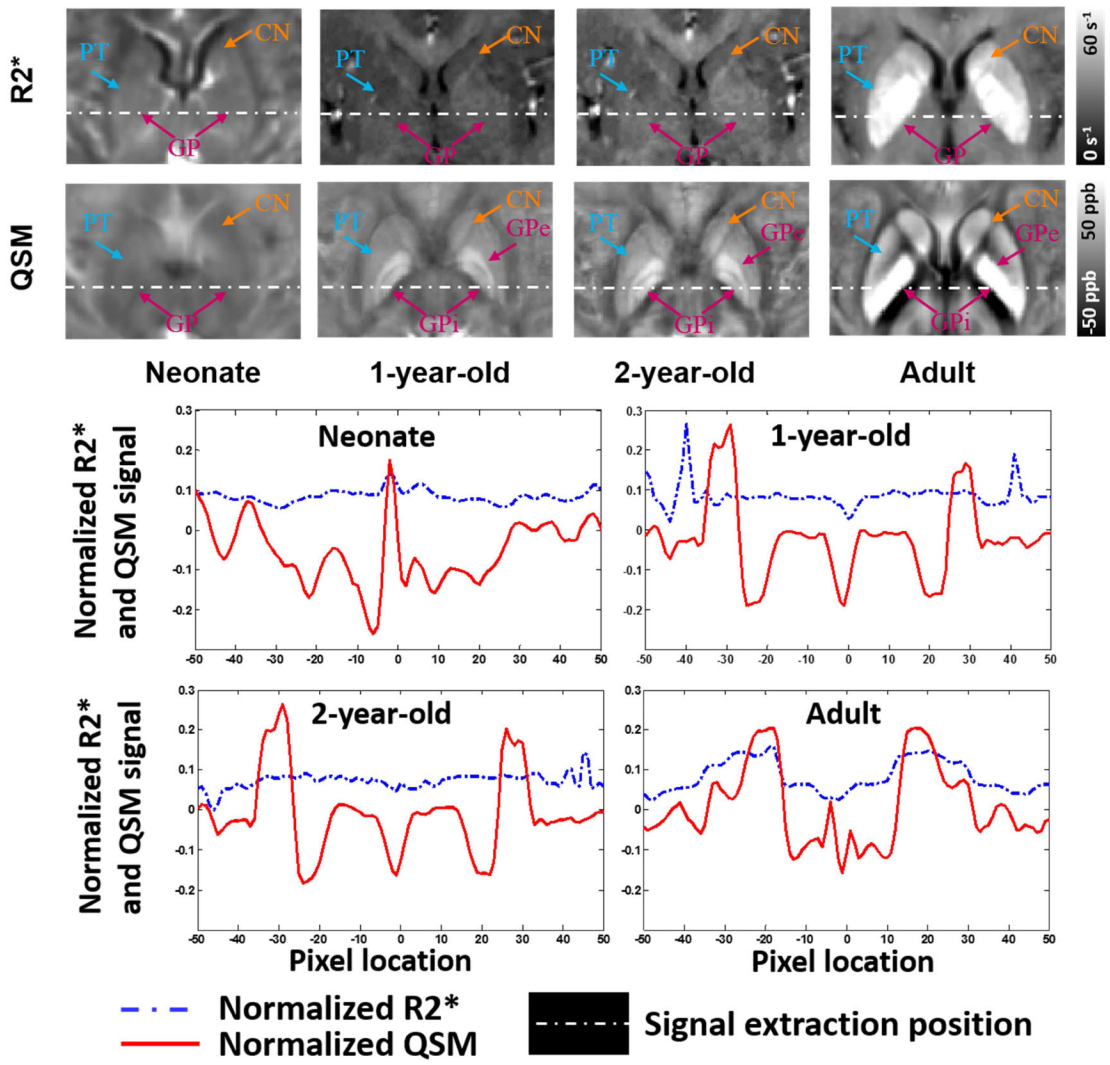


**Figure 6. Comparison of R2* and QSM templates for neonates, 1-year-old infants, 2-year-old infants and adults in basal ganglia.**

Top two rows: the R2* map and QSM axial section in basal ganglia indicating PT (putamen), GP (globus pallidus) and CN (caudate nucleus). Bottom two rows: Profile lines for the normalized R2* (blue dotted lines) and QSM (red lines) signal, which are extracted from each age-specific template as the white dotted line denoted (in top two rows).

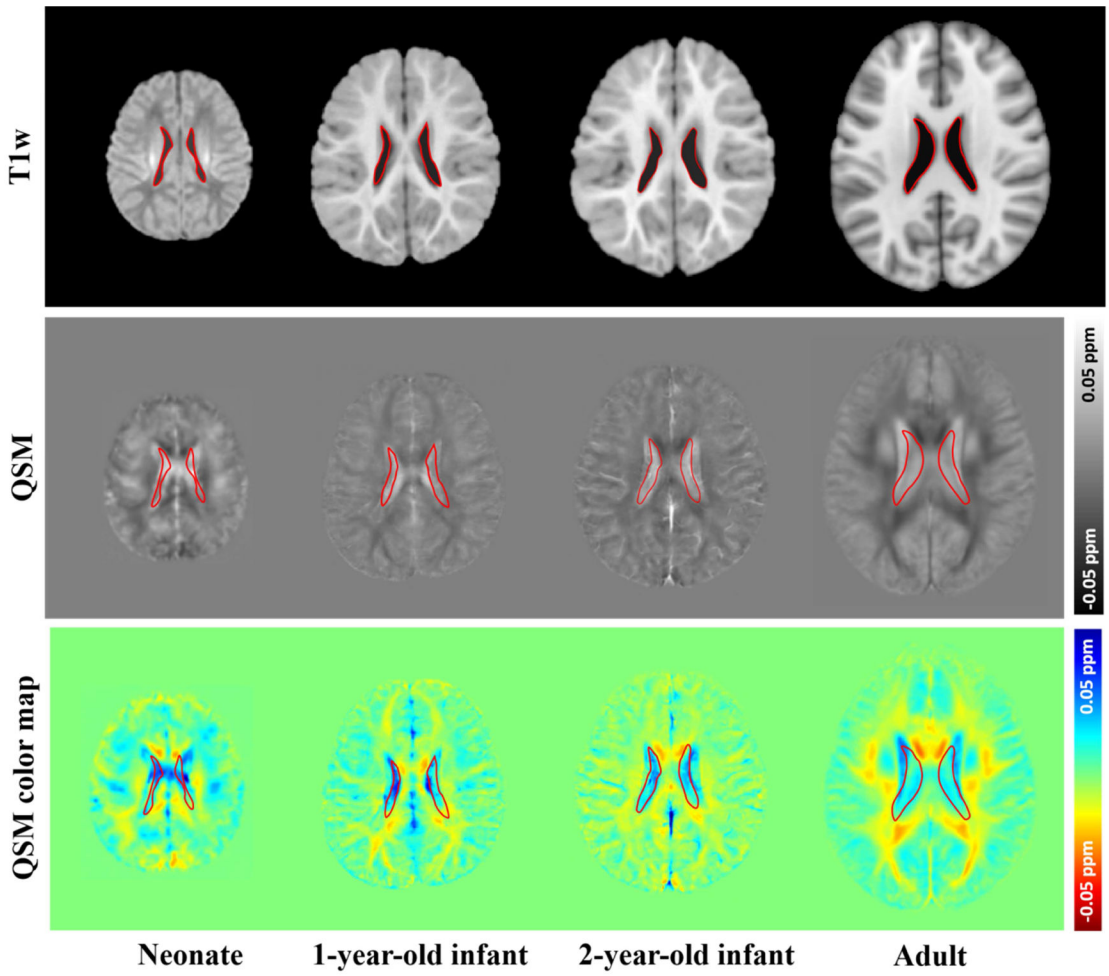


**Figure 7.**

Comparison of T1w and susceptibility maps (grey level map in middle row and color-coded map in bottom row) for neonates, 1-year-old infants, 2-year-old infants and adults. The CSF susceptibility shows gradual decrease in neonate and infant brains and is much higher than that of the adult brains.

**Table 1.**

Statistics of susceptibility in brain DGM nuclei for neonates, infants and adults [ppb].

| | Neonate | 1-year-old infant | 2-year-old infant | adult |
|---|---|---|---|---|
| Susceptibility in PT | −8.7±2.6 | 6.1±4.3 | 8.3±5.1 | 40.6±22.7 |
| Susceptibility in GP $\frac{\text{GPe}}{\text{GPi}}$ | −10.3±6.2 | 17.9±6.1 | 22.7±8.1 | 92.3±13.2 |
| | | 9.8±4.5 | 17.0±6.9 | 70.4±17.5 |
| Susceptibility in CN | −7.7±9.3 | 6.4±9.6 | 15.4±5.0 | 22.1±12.1 |
| Susceptibility in RN | −6.1±3.3 | −11.4±9.2 | 5.3±8.1 | 61.8±14.6 |
| Susceptibility in SN | −7.5±4.2 | −1.3±6.4 | 4.7±4.1 | 68.9±22.2 |

**Table 2.**

Statistics of susceptibility in brain CSF for neonates, infants and adults [*ppb*].

| | neonate | 1-year-old infant | 2-year-old infant | adult |
|---|---|---|---|---|
| Susceptibility in CSF | 58.0±18.6 | 25.4±8.1 | 15.3±6.5 | 6.4±7.0 |